JGR Atmospheres

RESEARCH ARTICLE
10.1029/2021JD035363

Evaluating the Variability of Surface Soil Moisture Simulated Within CMIP5 Using SMAP Data

Xuan Xi[1], Pierre Gentine[2], Qianlai Zhuang[1,3], and Seungbum Kim[4]

[1]Department of Earth, Atmospheric, and Planetary Sciences, Purdue University, West Lafayette, IN, USA, [2]Department of Earth of Environmental Engineering, Columbia University, New York, NY, USA, [3]Department of Agronomy, Purdue University, West Lafayette, IN, USA, [4]NASA Jet Propulsion Laboratory, Pasadena, CA, USA

Key Points:

- Land surface models tend to underestimate weekly to seasonal variability and overestimate seasonal to annual variability of soil moisture
- Simulated surface soil moisture variability is more closely related to climate conditions than soil texture
- Model-based soil moisture data may need to be improved to capture soil moisture variability on various frequency bands

Supporting Information:

Supporting Information may be found in the online version of this article.

Correspondence to:

Q. Zhuang,
qzhuang@purdue.edu

Citation:

Xi, X., Gentine, P., Zhuang, Q., & Kim, S. (2022). Evaluating the variability of surface soil moisture simulated within CMIP5 using SMAP data. *Journal of Geophysical Research: Atmospheres*, *127*, e2021JD035363. https://doi.org/10.1029/2021JD035363

Received 4 JUN 2021
Accepted 19 JAN 2022

Abstract There are significant biases and uncertainties in the simulated soil moisture with land surface models. Here we evaluate multimodel differences in Coupled Model Intercomparison Project Phase 5 (CMIP5) compared to Soil Moisture Active Passive (SMAP) products on different time scales. The variability of surface soil moisture (SSM) within three frequency bands (7–30 days, 30–90 days, and 90–365 days) after normalization is quantified using Fourier transform for the evaluation. Compared to the SMAP observations, the simulated SSM variability within CMIP5 is underestimated in the two higher frequency bands (by 72% and 56%, respectively) and overestimated in the lowest frequency band (by 113%). In addition, these differences concentrate in regions with larger SSM. Finally, these multimodel differences are found to be significantly correlated with mean climate conditions rather than soil texture. This study identifies the spatiotemporal distribution of the model deficiencies within CMIP5 and finds they are systematic in the long-term simulation on a global scale.

Plain Language Summary Soil moisture has been largely regarded as a key variable in Earth system and plays an important role in climate prediction. However, land surface models have large uncertainties in simulating soil moisture. This study identifies that (a) land surface models underestimate soil moisture variability on weekly to seasonal time scales and overestimate it on seasonal to annual time scales compared to a remote sensing observation, (b) both the underestimation and overestimation are concentrated in the wetter regions, and (c) the differences between these models and the observation are more closely related to vegetation condition and surface temperature than soil sand and clay content. Using satellite observed data, this study reveals the deficiencies of land surface models in simulating temporal variability of soil moisture, which will help improve the soil moisture predictability of these models.

1. Introduction

Soil moisture plays an essential role in land-atmosphere interactions and climate-change projections (Botter et al., 2007; D'Odorico et al., 2003; Green et al., 2019; Koster et al., 2004; Seneviratne et al., 2010). Due to the lack of enough in-situ measurements, soil moisture estimates on a global scale highly rely on parameterizations of the land surface models combined with climate data (Bonan, 1996; Koster et al., 2009). However, land surface models tend to have large uncertainties in simulating both magnitudes and spatiotemporal variabilities of soil moisture across different time scales (Katul et al., 2007; Nakai et al., 2014; Seneviratne & Koster, 2012; Seneviratne et al., 2006). For instance, a comparative analysis between four land surface models within the North American Land Data Assimilation System Project Phase 2 (NLDAS-2) shows the difference in their simulation skills and concludes that Noah and VIC are wetter while Mosaic and SAC are drier compared to the observations (Xia et al., 2015). Improving the model prediction of both soil moisture levels and their temporal variability has received an increasing interest in recent years.

Studies on soil moisture temporal variability at regional and global scales have focused on analyzing autocorrelations of soil moisture time series. The data were modeled as a first-order Markov process forced by a random precipitation time series (i.e., white noise) and an exponential damping term related to evapotranspiration losses (Delworth & Manabe, 1988). Based on this model, a red noise process can reasonably characterize the temporal variability of soil moisture, and the e-folding autocorrelation time scale of a red noise process can be used to quantify soil moisture variability (Delworth & Manabe, 1988). However, due to significant limitations in a strictly Markovian framework, a more complete framework based on a comprehensive soil moisture autocorrelation

analysis was proposed to understand soil moisture variability (Koster & Suarez, 2001). This framework was further revised by clarifying the effects of initial soil moisture variability (Seneviratne & Koster, 2012). The temporal spectrum and the integral time scale based on the autocorrelation function were also used as other memory metrics in studying soil moisture variability (Ghannam et al., 2016; Katul et al., 2007; Nakai et al., 2014). These methods are based on models where soil moisture is treated as a red noise process. A more recent study replaced the e-folding time scale of the red noise model with two new parameters, dividing soil moisture memory into short-term and long-term components (McColl et al., 2019).

The fifth phase of the Coupled Model Intercomparison Project (CMIP5; Taylor et al., 2012), which integrated a set of model experiments to improve our knowledge on climate change and climate variability, provides an opportunity for the multimodel assessment of land-atmospheric processes and variability. Evaluation of CMIP5 has been the ongoing interest of the community (Yuan et al., 2021). Although CMIP5 models have been used to investigate soil moisture-atmosphere interactions (Levine et al., 2016; May et al., 2015; Williams et al., 2012), to date, the temporal variabilities of soil moisture at short-term and seasonal scales are rarely evaluated within CMIP5 research activities. Many studies took soil moisture as an indicator to address dynamic climate questions, like drought (Huang et al., 2016; Ukkola et al., 2018) and soil moisture-evapotranspiration coupling (Berg & Sheffield, 2018), without explicitly providing soil moisture variability on different time scales. Several studies evaluated the temporal variability of soil moisture, but they did not perform analyses globally (Ruosteenoja et al., 2018; Yuan & Quiring, 2017). Some other works conducted a variability analysis of soil moisture at global scales but were conducted either on a coarse temporal resolution (Dirmeyer et al., 2013) or not within CMIP5 simulations (McColl et al., 2019).

Remote sensing technology provides global observations of soil moisture, such as the Soil Moisture Ocean Salinity (SMOS) mission (Kerr et al., 2001) and NASA's Soil Moisture Active Passive (SMAP) mission (Entekhabi et al., 2010). The soil moisture data of SMAP is surface soil moisture (SSM), defined as the moisture in the top ∼5 cm of the soil column. SMAP soil moisture meets mission requirements and matches well in situ SSM observations (Chan et al., 2016, 2018; Colliander et al., 2017, 2021). In addition, compared to two other soil moisture satellites, SMAP shows higher accuracy measured by a global average anomaly correlation over the majority of available land pixels (Chen et al., 2018) and high information content relative to other retrieval products of soil moisture (Kumar et al., 2018). In addition, a recent study shows that SMAP has good performance over irrigated and vegetated areas (Kim et al., 2020). The SMAP SSM can be used to explain land-atmosphere interactions over different spatiotemporal scales (Guillod et al., 2015; Tuttle & Salvucci, 2016).

This study takes advantage of the progress in soil moisture signal analysis, CMIP5 multimodel simulations, and satellite technology in estimating soil moisture discussed above to evaluate 17 land surface models within CMIP5 in soil moisture simulations using SMAP as the observational benchmark. The main research objective is to identify the deficiencies of these models in estimating global SSM on various time scales. Specifically, the simulated SSM variability is analyzed within three frequency bands: (1) weekly to monthly time scales (1/7–1/30 $days^{-1}$), (2) monthly to seasonal time scales (1/30–1/90 $days^{-1}$), and (3) seasonal to annual time scales (1/90–1/365 $days^{-1}$). Similar approaches to decomposing the time series into different frequency bands have been used to explain the precipitation variability and land-atmosphere interactions (Ruane & Roads, 2007; Wei et al., 2010). Further, the Fourier analysis (Thomson & Emery, 2014) is conducted to determine the frequency characteristics of the global SSM. In this way, we can identify the deficiencies of simulating SSM variability in these CMIP5 models, which are usually difficult to quantify in the time domain.

In Section 2, we first describe the model and observational data used. Then, we detail our methodology for variability analysis. In Section 3, we show the results of SMAP observations in the first part. In the second part, we perform comparative analyses on the multimodel differences within CMIP5 and further illustrate their correlations with mean SSM and four variables related to climate condition and soil texture. In the third part, we investigate uncertainties that may exist in this study and their effects on our analysis. In Section 4, we summarize our findings and discuss the research impacts and potential solutions to the model deficiencies we found.

2. Methods

2.1. Overview

We first describe how we collect the data from models within CMIP5 and SMAP observations. Second, we detail the methodology from data preprocessing to the final multimodel comparison. Specifically, Section 2.3 describes the preprocessing of SMAP products and CMIP5 simulations. Section 2.4 defines the normalized variability of SSM and how to get it within the three frequency bands. Next, Section 2.5 introduces the spectral slope of SSM within the three frequency bands and how to depict them as the color of noise. Finally, Section 2.6 describes how to perform multimodel comparative analysis with the SMAP observations and illustrates the significance test on the differences.

2.2. Data Organizing

In this study, we use the daily simulations from 17 CMIP5 models. The models are selected based on the availability of daily SSM outputs required for the spectral analysis (Table S1). To characterize SSM variability, we analyze the simulated SSM (top 10 cm; variable *mrsos* in the CMIP5 archive). We use only one ensemble member—"r1i1p1" (where *r* for realization, *i* for initialization, and *p* for physics) from the historical experiment.

Observation data of SSM are from NASA's SMAP mission. The SMAP satellite was launched in January 2015 and measured SSM globally every 2–3 days (Entekhabi et al., 2010). In this study, we use its Level 3 Radiometer Global Daily 36 km EASE-Grid Soil Moisture, Version 7, spanning 1 April 2015–2031 December 2020 (O'Neill et al., 2020). Since the air, vegetation, and near-surface soil are assumed to be in thermal equilibrium in the early morning hours for the radiometer soil moisture algorithm, there is more degradation in its 6 p.m. retrievals than 6 a.m. retrievals, but the degradation is small (Chan et al., 2018; O'Neill et al., 2018). Therefore, we use retrievals from both 6 a.m. descending and 6 p.m. ascending passes to best use the observational information. The Level 3 product is made using geophysical parameters derived from Level 1 and Level 2 products and is spatiotemporally re-sampled to the global cylindrical EASE-Grid 2.0 (Brodzik et al., 2012). In this projection, regardless of longitude and latitude, each grid cell has a nominal size of approximately 36×36 km^2, and the dimensions of the data arrays are 406 rows and 964 columns.

To analyze the relationship between soil texture and multimodel differences within CMIP5 compared to the SMAP observations, we use the Global Soil Dataset for Earth System Modeling (GSDE; Shangguan et al., 2014). GSDE provides 11 types of general soil profile information and 34 soil texture properties for eight depths. In this study, we use two main soil properties—sand content and clay content, to find their relationships with multimodel differences. GSDE provides two resolutions, that is, 30 s (~1 km) and 5 min (~10 km). We use the second one. In addition, all soil properties are separated into eight layers with different depths. Since we focus on surface soil moisture, we use the average of the first two layers (0–0.045 m and 0.045–0.091 m) for our analysis.

2.3. Data Preprocessing

Anomalous SMAP SSM values that do not range from 0.02 to 0.5 cm^3/cm^3 are removed. In addition, since SMAP does not provide global observations every day, its SSM retrievals are temporally discontinuous. Therefore, missing values are gap-filled to best use the daily resolution of SMAP data. We first fill SMAP data with a long term global daily soil moisture dataset (Yao & Lu, 2020), which is derived from AMSR-E and AMSR2 based on an Artificial Neural Network algorithm taking the SMAP standard SSM products as training targets (Yao et al., 2017, 2021). Next, we use moving average with a window of length 3 to fill the remaining missing values. Then, by using the autoregressive modeling, we fill the remaining gaps among the data with estimates extrapolated from forward and reverse autoregressive fitting of samples. Finally, we replace values less than 0.02 with 0.02 and larger than 0.5 with 0.5 (units: cm^3/cm^3) for the filled results to ensure that all SSM values are in a valid range. We validate this gap-filled SMAP data using in-situ soil moisture data of 16 sites from the International Soil Moisture Network (ISMN; Dorigo et al., 2011, 2013). Five sites are selected based on five latitude bands (Figure S2), and 11 sites are selected to represent 11 key plant function types (Figure S3). The latitude band and plant function type are both efficient and commonly-used ways to categorize the land surface. The statistical errors of the gap-filled SMAP data are close to (or even better than) the original SMAP product compared to in-situ SSM data within ISMN (Tables S4 and S5).

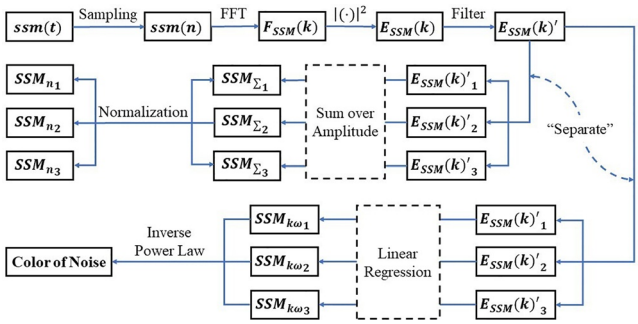

Figure 1. Steps to get the normalized variability of SSM (SSM_{n1}, SSM_{n2}, and SSM_{n3}, hereafter collectively referred to as SSM_n), and the spectral slope of SSM (SSM_{kw1}, SSM_{kw2}, and SSM_{kw3}, hereafter collectively referred to as SSM_{kw}) from the time series of SSM ($ssm(t)$). The number "1", "2", and "3" (hereafter being referred as i) represent three frequency bands in the order as weekly to monthly (7–30 days), monthly to seasonal (30–90 days), and seasonal to annual (90–365 days) time scales. $ssm(n)$ is the discrete series sampled from $ssm(t)$. $F_{SSM}(k)$ is the amplitude spectrum of SSM from $ssm(n)$ using Fast Fourier Transform (FFT). $E_{SSM}(k)$ is the power spectrum of SSM as the square of the absolute value of its amplitude. $E_{SSM}(k)'$ is the filtered $E_{SSM}(k)$ to a frequency band within 7–365 days. $E_{SSM}(k)'_i$ is $E_{SSM}(k)'$ being "separated" into the three frequency bands: weekly to monthly ($i = 1$), monthly to seasonal ($i = 2$), and seasonal to annual ($i = 3$). The sum of spectral amplitudes of SSM ($SSM_{\sum_i}$) and SSM_{kwi} is gotten from $E_{SSM}(k)'_i$ based on "sum over amplitude" and "linear regression" within in the ith frequency band, respectively. SSM_{ni} is gotten from $SSM_{\sum_i}$ based on normalization across the three frequency bands.

For the models within CMIP5, since the soil moisture simulations span decades or even centuries, some regions may show long-term linear trends on such time scales (Mudelsee, 2013). Since the Fast Fourier Transform (FFT) requires time series to be periodic, these long-term trends may result in boundary artifacts that would introduce errors into the power spectrum when performing Fourier analysis. Therefore, we remove these trends by subtracting an optimal (least squares) fitted linear regression from original data so that the time series after detrending has a mean value of zero. Thus, we focus on the intra-annual fluctuations of the SSM time series. This detrending process is not performed on the SMAP observation since its temporal coverage is too short of having significant long-term linear trends.

2.4. Normalized Variability of SSM

Normalized variability of SSM (SSM_n) for CMIP5 models and SMAP observations are both calculated for comparison. SSM_n indicates the proportion of the temporal variability of SSM within the three frequency bands. We aim to use SSM_n to evaluate the model performance on capturing the temporal variability over different time scales. The procedures to get SSM_n from time series of SSM ($ssm(t)$) are shown in Figure 1 (see Figure S1 as a detailed version with an example). Here, we explain the steps to process SSM_n in detail.

The computation of SSM_n for models and observation is the same. It is based on the Fast Fourier Transform (FFT), a faster algorithm for the Discrete Fourier Transform (DFT). They decompose the time series into orthogonal sinusoidal frequency components so that the variability within each component can be investigated separately. The basic mathematical theory for DFT and FFT and related spectrum analyses can be found in Text S1. All computations and statistical analyses in this study are programmed in MATLAB (http://www.mathworks.com/).

First, we use FFT to get the amplitude spectrum of SSM ($|F_{SSM}(k)|$) from $ssm(n)$, which is the discrete series sampled from $ssm(t)$ with the sampling number (N; i.e., the number of days). Since the spectrum is symmetrical about the Nyquist frequency ($f_s/2$, where f_s is sampling frequency as 1 day^{-1} here), we only use half spectrum (sampling points from 1 to $N/2$ without the first sampling point that is the DC component). The frequency corresponding to each sample is the product of its normalized frequency and the frequency resolution (Δf).

Then we get the power spectrum of SSM based on its amplitude spectrum as $E_{SSM}(k) = |F_{SSM}(k)|^2$. The frequency of $E_{SSM}(k)$ ranges from 1/2 to $1/N$ day^{-1}. In this study, we filter the spectrum to a frequency band within 7–365 days due to the limitations of the satellite data. On the one hand, missing values filling during the data preprocessing may introduce high-frequency variability as noises to the observation, which usually do not exist in models. Therefore, we remove the spectrum with frequencies higher than 1/7 days^{-1} to make models and observations more comparable by smoothing the observational data. On the other hand, unlike CMIP5 models with multi-decade records, the temporal coverage of SMAP observations is less than 6 years. This is not long enough to make reasonable analyses on inter-annual time scales, and thus we also remove the spectrum with frequencies lower than 1/365 days^{-1}. In this way, we restrict our investigation within a weekly to annual frequency band by using a low-pass filter and a high-pass filter with the cutoff frequency as 1/7 days^{-1} and 1/365 days^{-1}, respectively.

Next, we separate the filtered $E_{SSM}(k)$ ($E_{SSM}(k)'$) into three frequency bands: weekly to monthly (7–30 days), monthly to seasonal (30–90 days), and seasonal to annual (90–365 days), defining that the number of days within one week, one month, one season, and one year, is 7, 30, 90, and 365, respectively. Thus, the three frequency bands represent weekly to monthly time scales, monthly to seasonal time scales, and seasonal to annual time scales, respectively. Divided by the total spectral power of $E_{SSM}(k)'$, the spectral power for each frequency band is normalized as:

$$SSM_{n_i} = \frac{\sum_j E_{SSM\,i}(k_j)'}{\sum_{i=1}^{3}\sum_j E_{SSM\,i}(k_j)'} \quad (1)$$

where $E_{SSM\,i}(k_j)'$ represents the spectral power of SSM for the jth frequency in the ith frequency band after filtering, i is the ordinal number representing the three frequency bands defined before in the order from high to low, and j is the ordinal number of each frequency within each frequency band. Thus, we denote SSM_{ni} as the normalized variability of SSM in the ith frequency band (e.g., SSM_{n1} is the normalized variability of SSM within weekly to monthly time scales). In this way, SSM_{ni}, as a value between 0 and 1, indicates the proportion of the spectral power of SSM time series in the ith frequency band. According to the Parseval theorem (Weisstein, 2019), the spectral power of SSM in the time domain and the frequency domain are equivalent. Therefore, we use SSM_{ni} to identify the major frequency behaviors of SSM sets for temporal variability analysis.

2.5. Analysis of Spectral Slope of SSM

The spectral slope exhibits characteristics of the soil moisture's physical behavior. First, we normalize all spectra by the variance of their respective temporal range to avoid that the spectra from high variance regions might overwhelm the spectra from low variance regions (Delworth & Manabe, 1988). Then, based on the least-squares approach, we fit a linear regression for the spectral power values corresponding to all frequencies within each frequency band and use the slope of the fitted line to analyze the spectral slope (see Table S6 as statistical errors of the linear regression). In this way, each spatial pixel has three spectral slopes corresponding to the three frequency bands.

Considering SSM as power-law noise signals, their spectral densities vary as inverse frequency, more precisely are proportional to $1/f^{\beta}$, where β is the inverse number of the spectral slope (Bourke, 1998). In this way, the color of noise, which is related to the power spectrum of noise signals, can be used to indicate the spectral slopes of SSM ($SSM_{k\omega}$). The basic theory of the color of noise can be found in Text S2.

The noise colors can be divided into several types according to the slope of their power spectral density. In this study, we use white noise and five main colored noises (violet, blue, pink, red, and black noise) to characterize SSM_{kwi} in the ith frequency band. The corresponding spectral slope (the opposite of β in inverse power law $1/f^{\beta}$) of violet, blue, white, pink, and red noise (or Brownian noise) is 2, 1, 0 (i.e., the spectral density of white noise is flat), -1, and -2, respectively, and the spectral slope of black noise is smaller than -2. The smaller the spectral slope in the frequency domain, the longer the memory of the signals that are represented as different colors of noise (excluding violet and blue noise). Therefore, we use this categorical $SSM_{k\omega}$ to characterize the memory of SSM on different time scales. The steps to get $SSM_{k\omega}$ are also shown in Figure 1.

2.6. Analysis of Differences Between Models and Observations

We evaluate multimodel differences of SSM_n and $SSM_{k\omega}$ within CMIP5 compared to SMAP observations by subtracting the observation data from the average of the 17 models. In addition, we calculate the coefficient of variation across the 17 models to show the degree of the statistical dispersion of SSM_n.

The spatial resolution and the land cover between models and observations, as well as among models themselves, are different. Therefore, we first use the spatial resolution of SMAP (36×36 km) as the reference and project all matrices to this "standard" spatial resolution based on a nearest neighbor binning:

$$\mathrm{D}(m, m') = \underset{p,q}{\operatorname{argmin}} \left| \left(m'_p - m_p\right) + \left(m'_q - m_q\right) \right| \quad (2)$$

where $\mathrm{D}(m, m')$ is the shortest distance between the non-SMAP pixel and the SMAP pixel, m and m' represents SMAP pixels and non-SMAP pixels, p and q are latitude and longitude to the corresponding pixel, respectively. We then adjust all re-gridded matrices to have the same land cover as the result based on SMAP data. Specifically, for each matrix, we remove its corresponding pixels without a value (i.e., shown as "NaN") in SMAP data. For pixels with values in SMAP data but no values in other matrices, we fill them based on the mean value of their nearest neighbors. In this way, all results have the same spatial resolution and land cover and can be compared with each other.

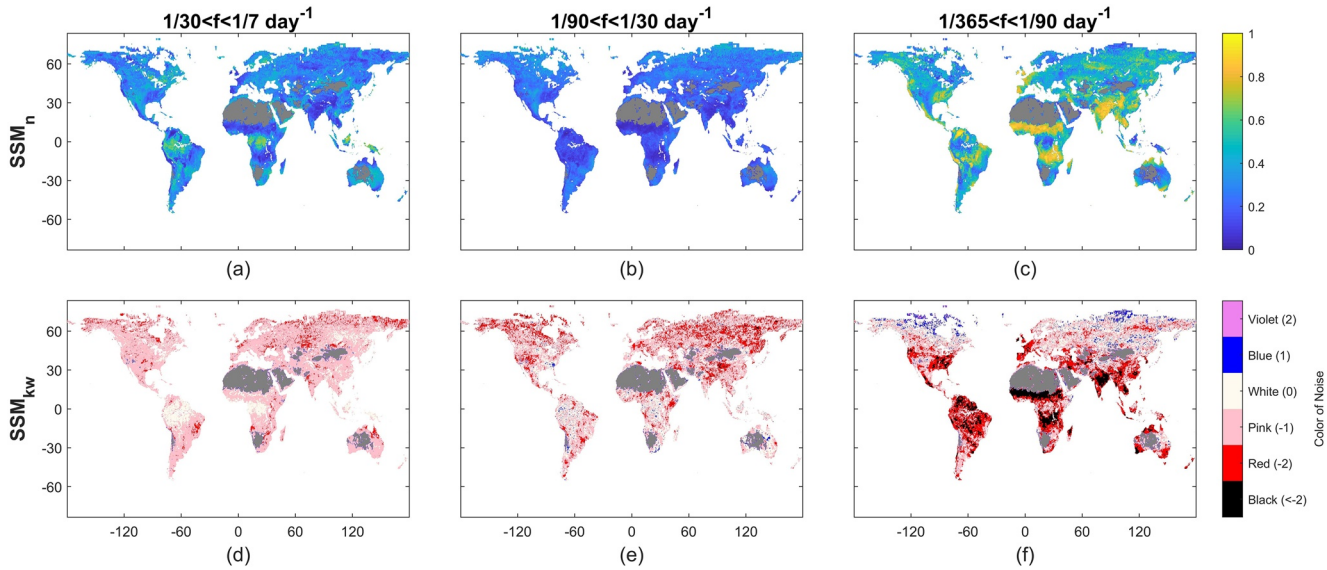

Figure 2. SSM_n (Figures a–c) and $SSM_{k\omega}$ (shown as noise color, Figures d–f) of SMAP observations over the three frequency bands. Dark gray parts are regions with $\overline{SSM}_n$ less than 0.1. The colors in Figures d–f represent the color of noise referring to the power spectra of SSM, and the number in brackets after color names is the spectral slope of power-law noise corresponding to each noise color. For all subsequent results, including Figure 2, the three columns from left to right represent the weekly to monthly frequency band ($i = 1$), the monthly to seasonal frequency band ($i = 2$), and the seasonal to annual frequency band ($i = 3$).

In addition, we perform a significance test on these differences and depict it using stippling. The reason is that multimodel differences in some regions may be caused by only a few models or even one model. These differences with less significance will not be considered. The significance here is defined as the ratio of the number of models with the same sign as average differences to the number of total models for each pixel. On the final maps, stippling shows the regions that passed the significance test of 100% (i.e., all 17 models agree on the sign of average differences) and 80% (i.e., 14 of the 17 models agree on the sign of average differences), respectively. We also remove regions with $\overline{SSM}_n$ less than 0.1 (shown as dark gray on the maps), where $\overline{SSM}_n$ defined as the observational mean SSM after spatiotemporal normalization (Figure S4). The reason is that the absolute values of SSM in these regions are too small to be investigated reasonably on its temporal variability.

3. Results and Discussion

3.1. Temporal Vairiabilities of SMAP SSM

Among the three frequency bands, the observational SSM_n concentrates more in the seasonal to annual frequency band for most regions, especially southern Asia, western Europe, and regions around 10°N/S in Africa. This indicates that SSM has a large variability on time scales longer than seasonal scales. For time scales shorter than seasonal scales, SSM_n concentrates more in the weekly to monthly frequency bands, especially in Australia and the regions near the equator (Figures 2a–2c).

The observational SSM_{kw} across the three frequency bands demonstrate that the spectrum of SSM time series is mainly shown as red and pink noise on a global scale (Figures 2d–2f), which means that low-frequency periodic components dominate the contribution to its variance. This is consistent with the findings based on SSM_n. Besides, the SSM spectra decay less rapidly in the weekly to monthly frequency band (Figure 2d) and more rapidly in the seasonal to annual frequency band (Figure 2f), indicating that SSM has more randomness on time scales shorter than monthly and more memory on time scales longer than seasonal scales. In addition, the spatial distribution of SSM_{kw} further displays the spatial variability of SSM_n within each frequency band as discussed above. In the weekly to monthly frequency band, regions with larger SSM_n show as white noise, meaning that the contribution to its variance is equal across all frequencies in this band (Figures 2a and 2d). In the seasonal to annual frequency band, regions with larger SSM_n show as black noise, meaning its variances are more dominated by the low-frequency periodic components (Figures 2c and 2f).

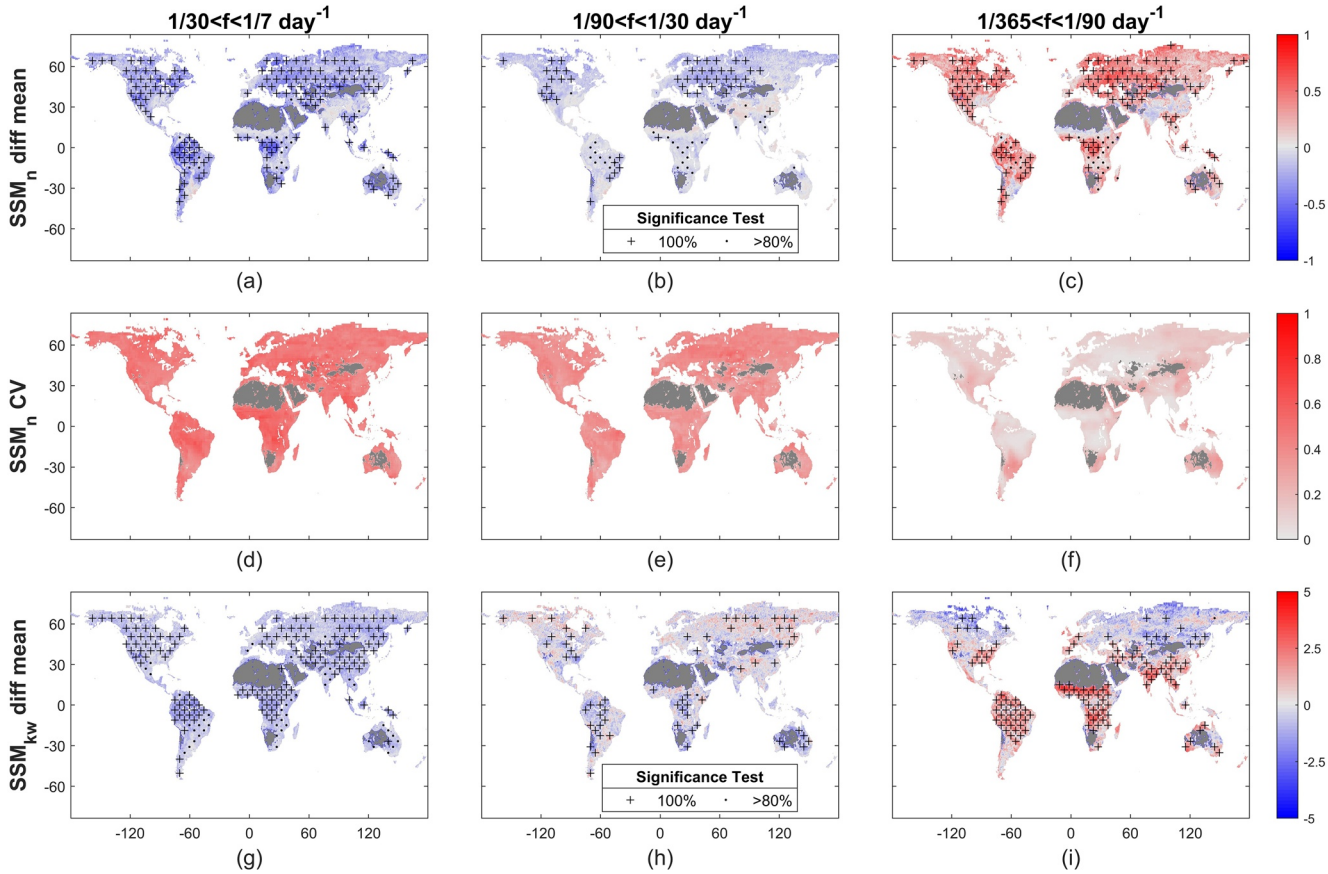

Figure 3. Comparisons of SSM variability between the models from CMIP5 and the SMAP observations in the three frequency bands. Figures a–c is the average difference of models' SSM_n compared to the observation, Figures d–f is the coefficient of variation (CV) of SSM_n across all models, and Figures g–i is the average difference of models' SSM_{kw} compared to the observation. For Figures d–f, the CV of SSM_n is calculated by the standard deviation of SSM_n divided by their average in each frequency band and then normalized between zero and one across the three frequency bands. For average differences of SSM_n (Figures a–c) and $SSM_{k\omega}$ (Figures g–i), "+" and "." stippling represents the region that passes a 100% significance test and an 80% significance test, respectively. Dark gray parts are regions with $\overline{SSM_n}$ less than 0.1.

3.2. Comparison Between CMIP5 Simulations and SMAP Observations

Figures 3a–3c shows the average differences for SSM_n of CMIP5 models compared to SMAP observations. A significance test is performed and depicted using stippling. Here, the "+" stippling means the region passes a 100% significance test, and the "." stippling means the region passes an 80% significance test. Therefore, we only focus on the regions with stippling. For most regions, the multimodel differences are negative in the two higher frequency bands and positive in the lowest frequency band. This means that the SSM variability of CMIP5 models is smaller on time scales shorter than seasonal and larger on time scales longer than seasonal, compared to SMAP observations. Among the three frequency bands, the average SSM_n difference is largest in the seasonal to annual frequency band (0.4003 and 0.3240 with 100% and 80% significance) and smallest in the monthly to seasonal frequency band (−0.1574 and −0.1025 with 100% and 80% significance; Table 1). For all three frequency bands, the average SSM_n differences are larger in Central and Eastern North America, Eastern Europe, Central Asia, and regions near the equator. Since the average SSM_n in each frequency band is different, here we use its coefficient of variation (CV) to see the degree of the variations among these models and normalize them over the three frequency bands (Figures 3d–3f). For most regions, the normalized CV is largest in the weekly to monthly frequency band and smallest in the seasonal to annual frequency band (see Table S7). Therefore, on time scales shorter than seasonal where models' SSM variability is smaller, a more extensive intermodel spread exists, meaning that the models exhibit significant variances in SSM variability estimation. On the other hand, on time scales longer than seasonal where models' SSM variability is larger, the estimates of SSM variability are similar across models, suggesting a systematic deficiency of land surface models in simulating a long-term variability.

Table 1
Multimodel Differences of SSM_n Within CMIP5 Compared to SMAP Observations

Significance	100% significance test			80% significance test		
Frequency band (day^{-1})	1/7–1/30	1/30–1/90	1/90–1/365	1/7–1/30	1/30–1/90	1/90–1/365
BCC-CSM1.1	−0.2060	−0.1065	0.2666	−0.1462	−0.0377	0.1713
BNU-ESM	−0.2690	−0.1332	0.3626	−0.2184	−0.0837	0.2919
CanESM2	−0.2997	−0.1579	0.4045	−0.2450	−0.0941	0.3214
CNRM-CM5	−0.2705	−0.2111	0.4376	−0.2177	−0.1525	0.3581
CSIRO-Mk3.6	−0.3189	−0.1995	0.4690	−0.2662	−0.1311	0.3844
GFDL-CM3	−0.2810	−0.1492	0.3908	−0.2328	−0.1030	0.3236
GFDL-ESM2G	−0.2750	−0.1405	0.3768	−0.2260	−0.0947	0.3077
GFDL-ESM2M	−0.2751	−0.1406	0.3778	−0.2257	−0.0938	0.3075
HadGEM2-CC	−0.3095	−0.1600	0.4263	−0.2593	−0.1057	0.3533
HadGEM2-ES	−0.3086	−0.1611	0.4252	−0.2590	−0.1063	0.3527
Institute for Numerical Mathematics	−0.2814	−0.1603	0.3937	−0.2244	−0.1006	0.3127
MIROC5	−0.2888	−0.1348	0.3829	−0.2372	−0.0867	0.3111
MIROC-ESM	−0.2923	−0.1446	0.3993	−0.2392	−0.0948	0.3227
MIROC-ESM-CHEM	−0.2932	−0.1460	0.4011	−0.2402	−0.0963	0.3254
MRI-CGCM3	−0.3164	−0.1997	0.4689	−0.2644	−0.1396	0.3912
MRI-ESM1	−0.3157	−0.1991	0.4670	−0.2638	−0.1385	0.3893
NorESM1-M	−0.2634	−0.1319	0.3548	−0.2111	−0.0830	0.2832
Average (±1SD)	−0.2861 ± 0.0265	−0.1574 ± 0.0282	0.4003 ± 0.0482	−0.2339 ± 0.0279	−0.1025 ± 0.0260	0.3240 ± 0.0498
Observation	0.3971	0.2789	0.3542	0.3465	0.2317	0.4254

We also evaluate multimodel differences of $SSM_{k\omega}$ compared to SMAP observations, with negative differences meaning that modeled spectra decay more rapidly and vice versa (Figures 3g–3i). Compared to observational SSM spectra, modeled decay more rapidly in the weekly to seasonal frequency bands and less rapidly in the seasonal to annual frequency band. This indicates that the differences between CMIP5 simulations and SMAP observations from the short-term variability to the long-term variability behave in a non-linear way. From Figures 3a–3c, we found that the turning point of this change can be indicated by the seasonal time scale (i.e., 1/90 $days^{-1}$), suggesting that the seasonal time scale is significant in characterizing the long-term memory of SSM.

The multimodel SSM_n differences compared to the SMAP observations are further analyzed with the mean SSM on a global scale. To make a trade-off between high significance and enough samples, we use the differences passing an 80% significance test. Figure S4 shows the global distribution of the observational mean SSM after spatiotemporal normalization ($\overline{SSM}_n$). From Figures 4a–4c, for all three frequency bands, the differences mainly concentrate in wetter regions with larger $\overline{SSM}_n$ (about 60%–90%), which is more evident in the weekly to monthly frequency band and seasonal to annual frequency band where SSM_n differences are larger. This finding is consistent with the result shown in Figure 5. From an average latitudinal perspective, larger differences of SSM_n are seen in regions near the equator and higher latitudes (especially regions around 45°N/S), where the mean SSM contents are higher (Figure 5d). On the other hand, SSM_n differences are smaller in regions around 15°N/S and 30°N/S, where there are lower mean SSM contents (Figure 5d). Besides, from Figures 5a–5c, for latitudinal average SSM_n in lower latitudes, model estimations can basically capture the trend of the observation. The differences in these regions mainly come from the differences in amplitude, which can be resolved more easily by, for example, parameter optimization (Houska et al., 2015). However, differences in higher latitudes are not only shown as the biases in amplitude but also the trend with latitudes. Therefore, these differences may be not only due to the parameterization issues but also the deficiencies in algorithms that model important physical processes, suggesting larger difficulties in simulating soil moisture dynamics that need more effort to increase the interpretability. For the intermodel spread of SSM variability estimates, Figures 4d–4f shows that there is no significant statistical correlation between its CV and SSM content. To sum up, for SSM variability compared to

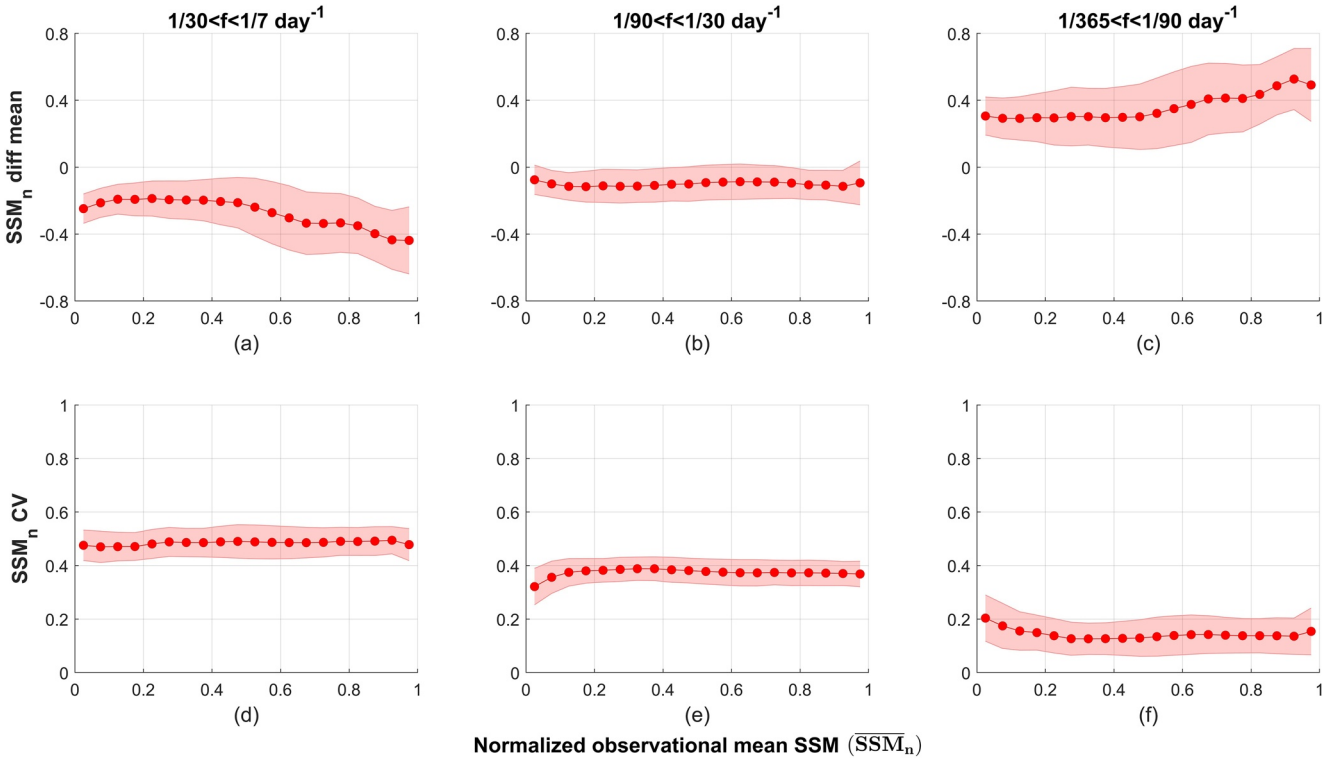

Figure 4. Comparison of SSM_n with $\overline{SSM}_n$ in the three frequency bands. Figures a–c shows the average difference of SSM_n between the models from CMIP5 and the SMAP observations, and Figures d–f shows the normalized coefficient of variation (CV) of SSM_n across all models. The red shading represents + /− one standard deviation. $\overline{SSM}_n$ is separated into 20 bins of equal size (i.e., 0.05 for each bin), then the mean of SSM_n differences and the CV of SSM_n located in each bin (corresponding to the range of $\overline{SSM}_n$) were separately calculated for each frequency band. Differences in this figure are the values passing an 80% significance test. All values in the regions with $\overline{SSM}_n$ less than 0.1 are removed.

SMAP observations, these models from CMIP5 show underestimated differences as "lower bias, higher variance" in the two higher frequency bands and overestimated differences as "higher bias, lower variance" in the seasonal to annual frequency band. These differences are mainly concentrated in wetter areas and are more challenging to solve in higher latitudes if considering all of them as model biases.

The multimodel differences of SSM_n have been found to be tightly related to the mean SSM (Figures 4a–4c). Apart from that, it is also necessary to identify their correlations with climate conditions and soil texture, which affect SSM closely. Here, we use the data of vegetation water content, surface temperature, and two main soil properties—sand content and clay content, to evaluate this dependence. Figures S5 and S6 show the global distribution of the mean vegetation water content ($\overline{Veg}_n$) and surface temperature ($\overline{T}_n$) after spatiotemporal normalization, respectively. Figure S7 shows the global distribution of soil sand content and clay content for the first two layers from the GSDE. We use the mean values of these two layers after spatiotemporal normalization ($\overline{Sand}_n$ and $\overline{Clay}_n$) to see their relationship with multimodel differences. Same as Figure 4, here we use the differences passing an 80% significance test (see Figure S8 as the corresponding correlation analysis with the differences passing a 100% significance test). The multimodel differences of SSM_n show an evident correlation with both $\overline{Veg}_n$ and $\overline{T}_n$. For $\overline{Veg}_n$, the differences of SSM_n basically increase with the increase of $\overline{Veg}_n$ linearly, except for the monthly to seasonal frequency band (Figures 6a–6c). For $\overline{T}_n$, the differences of SSM_n basically increase with the decrease of $\overline{T}_n$ linearly, except for the weekly to monthly frequency band (Figures 6d–6f). This indicates that these multimodel differences are basically positively correlated to vegetation water content while negatively correlated to surface temperature. On the other hand, there are no clear correlations between SSM_n differences and soil texture across all frequency bands (Figures 6g–6l). This means that it is not the soil itself that leads to the model differences within CMIP5, but rather that models did not represent other processes regulating soil moisture, such as vegetation which regulates the transpiration and long-term soil moisture dynamics (Kennedy

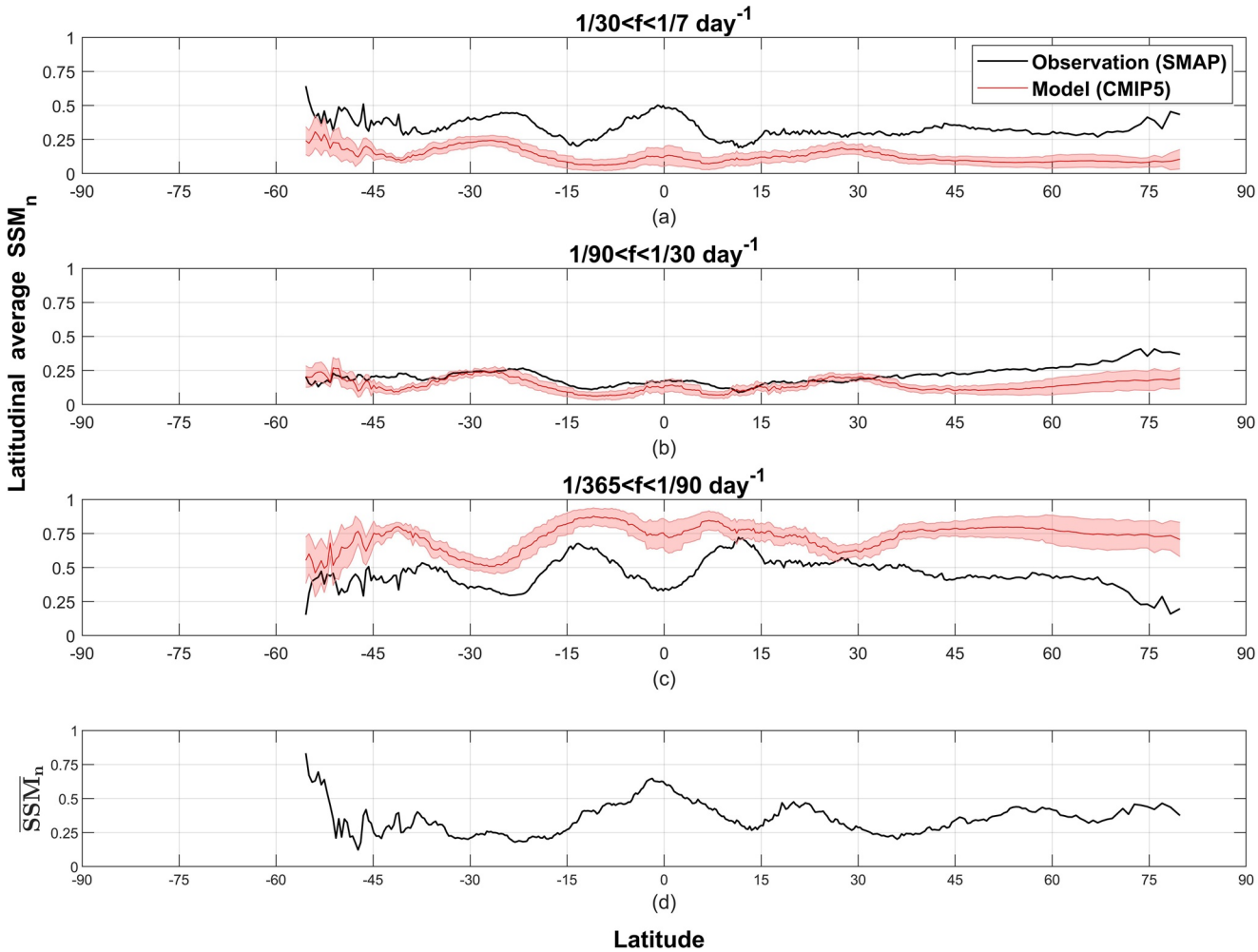

Figure 5. Latitudinal average SSM_n for CMIP5 models and the SMAP observations in the three frequency bands (Figures a–c) and latitudinal average $\overline{SSM}_n$ (Figure d). Black lines are results from SMAP observations, and red lines are results of CMIP5 models. The red shading represents $+/-$ one standard deviation. The mean values of SSM_n and $\overline{SSM}_n$ for each latitude are calculated as the y values. Average SSM_n of models in this figure are values passing an 80% significance test. All values in the regions with $\overline{SSM}_n$ less than 0.1 are removed.

et al., 2019). For instance, plant water stress based on plant hydraulics has shown superior results when compared to typical water-stress responses (Kennedy et al., 2019), especially on seasonal time scales.

3.3. Uncertainty Analysis of SSM Variability

In this study, since the SMAP data is non-continuous on the daily time scale, we fill the missing values before performing Fourier analysis. We first use a moving window to fill missing values and then use the autoregressive modeling to fill the remaining gaps. Although we have validated this filled SMAP data with in-situ soil moisture data from ISMN, the in-situ observations still can not cover all pixels on a global scale. Since we do not have such observational data for those missing values, this filling process may introduce uncertainties to the subsequent results. Here we check these uncertainties to quantify how much confidence we can have for using the filled SMAP data as the observations. There are four parameters in the filling: "moving method", "moving window length", "maximum length of prediction sequences", and "autoregressive model order". We separately change one of them (for the "moving method", we change from mean to median; for the other three, we change the values by 100%) and compare the SSM_n obtained from the two filling data. We find that "moving window length" is the parameter that will introduce the most uncertainties (see Figure S9). Therefore, it is most critical to constrain uncertainties made by this parameter during the gap filling.

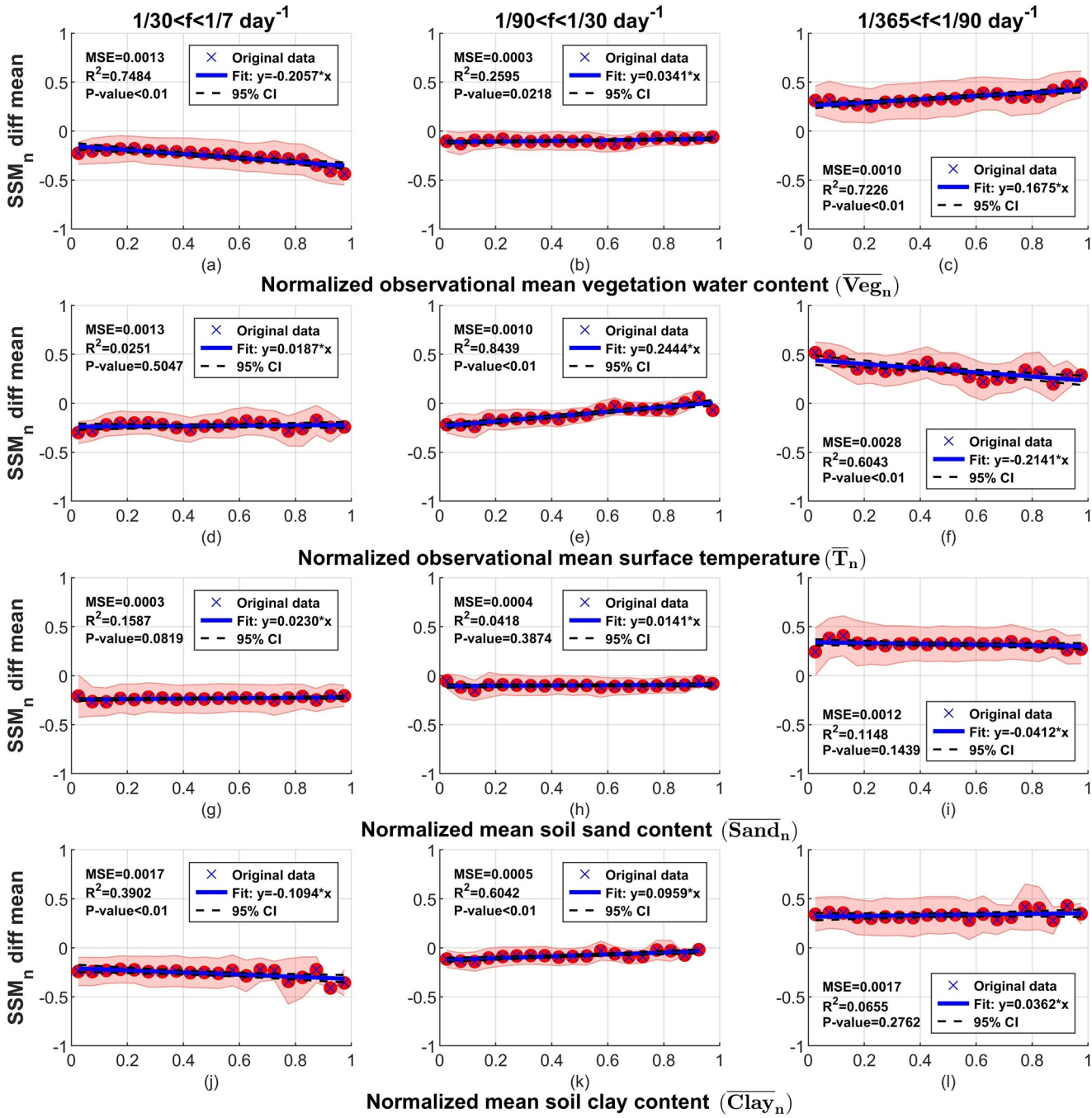

Figure 6. Multimodel mean differences of SSM_n between models within CMIP5 and SMAP data with $\overline{Veg_n}$ (Figures a–c), $\overline{T_n}$ (Figures d–f), $\overline{Sand_n}$ (Figures g–i), and $\overline{Clay_n}$ (Figures j–l). The red shading represents + /− one standard deviation. The blue crosses are exactly the red dots that are SSM_n difference in each bin. The solid blue lines represent the fitted linear regression lines based on the blue crosses. The black dashed lines represent the bounds of the 95% confidence interval (CI). Differences in this figure are the values passing an 80% significance test. All values in the regions with $\overline{SSM_n}$ less than 0.1 are all removed.

We change the "moving window length" as 3, 5, 7, 9 while fixing the other three parameters to compute observational SSM_n, respectively. We find it will cause a significant change to SSM_n in the first and third frequency bands (see Table 2)—the larger the moving window length, the smaller SSM_n of the first frequency band, and the larger SSM_n of the third frequency band. The reason is that the moving window here plays a role like a low-pass filter that will smooth the time-series signal, with a longer window decreasing more components of high frequencies. However, even the window length increases to 9 (i.e., filling the missing value as the mean of the previous four

Table 2
Observational and Model Average Normalized Variability of SSM (SSM_n) in Three Frequency Bands Based on Three Observational Data Sets with Different Moving Window Lengths

Data sets	Moving window length (#)	Normalized variability of SSM (SSM_n) in three frequency bands		
		1/7–1/30 days^{-1} (weekly to monthly)	1/30–1/90 days^{-1} (monthly to seasonal)	1/90–1/365 days^{-1} (seasonal to annual)
SMAP (04/01/2015–12/31/2020)	3	0.3059	0.2198	0.4743
	5	0.2811	0.2272	0.4917
	7	0.2577	0.2330	0.5093
	9	0.2234	0.2396	0.5370
SMAP & AMSR-E/2 (04/01/2015–12/31/2020)	3	0.3216	0.2093	0.4692
	5	0.3014	0.2170	0.4816
	7	0.2786	0.2240	0.4974
	9	0.2557	0.2293	0.5149
SMAP & AMSR-E/2 (06/01/2002–12/31/2020)	3	0.3480	0.2452	0.4068
	5	0.3488	0.2478	0.4033
	7	0.3437	0.2519	0.4044
	9	0.3356	0.2569	0.4075
Model average in CMIP5		0.1159	0.1427	0.7414

and the last four samples), the observational SSM_n is still larger than the modeled in two higher frequency bands and smaller than the modeled in the lowest frequency band, which is qualitatively consistent with our previous results (Figures 3a–3c).

Since the sampling frequency of SMAP is once per two or three days and may even be less due to its orbital geometry, there are a large number of missing values within the temporary coverage in this study. Therefore, we first fill the SMAP data with a long-term global daily soil moisture dataset based on AMSR-E/2 (hereafter referred to as "AMSR-E/2 data", see Section 2.3). However, this filled data are still discontinuous at the daily time scale. So, we also perform the same test of "moving window length" on the gap-filled SSM data that is used for subsequent analyses. From Table 2, we can see that adding this AMSR-E/2 data to the original SMAP product can help constrain uncertainties during the missing value filling, especially for the first and third frequency bands. Besides, adding AMSR-E/2 data tends to increase SSM_n in the first frequency band and decrease it in the third frequency band. This means that, with more observation-based values, observational SSM_n will increase on shorter time scales and decrease on longer time scales. Therefore, we choose to use "3" as the "moving window length" for our analysis.

In addition, due to the limited time span of SMAP currently, we only use less than six years' data (2102 days) to evaluate the temporal variability of SSM. There might be insufficient degrees of freedom in such a period to provide significant results on longer time scales. Therefore, we combine SMAP and AMSR-E/2 data as a long-term global SSM series (6789 days) to assess SSM_n and also perform the same test of "moving window length" on it. From Table 2, observational SSM_n shows extremely fewer uncertainties based on this long-term series and is close to what we used in this study. This provides much confidence for our long-term results, especially for the third frequency band. Besides, SSM_n on the long-term series increases a bit in the first frequency band compared to that we used for comparative analysis, which further validates our method of gap filling.

Apart from the filling during data preprocessing, the interpolation during intermodel computation may also introduce uncertainties since the spatial resolution of all models are much coarser than the "standard" spatial resolution (36 × 36 km, see Section 2.6). To quantify these uncertainties, we compared the difference between SMAP and CMIP5 models on this "standard" spatial resolution with another spatial resolution as 1° × 1° (Figure S10), which is between the resolution of SMAP and CMIP5 models. We further calculated the mean and standard deviation of SSM_n differences for each frequency band on the two resolutions (Table S8). The results are very close to each other. We thus concluded that the SSM variability of CMIP5 models is smaller in higher frequency

bands (weekly to seasonal) and larger in the lower frequency band (seasonal to annual) compared to SMAP observations. Moreover, we also conducted the significance test to constrain the possible uncertainties as much as possible. All statistical correlation analyses in this study are based on the multimodel differences passing a high significance test (more than 80% as Figure 6 and equal to 100% as Figure S8), ensuring that a systematic performance in land surface models is shown.

Finally, this study conducts comparative assessments of CMIP5 models and uses SMAP products as the observations. However, even though SMAP has been demonstrated to meet its performance target, it still has its own deficiencies on a global scale. For example, its soil moisture retrievals in heavily vegetated areas such as forests will exist some errors due to the simplification in the representation of the vegetation effect (Entekhabi et al., 2014), and retrievals from the presence of water bodies, snow, and frozen soil can be potentially impacted by radio frequency interference (McColl et al., 2017). Besides, SMAP SSM products may not be reliable in an Arctic tundra environment (Wrona et al., 2017). In addition, there are differences in global SSM retrievals among different satellite products (Burgin et al., 2017), suggesting uncertainties in the measurement of global SSM observation. Therefore, when performing comparative evaluations with model estimations, the biases in observational data themselves should also be taken into consideration. In addition, from our gap-filled SMAP validation compared to sites within ISMN (Figures S2 and S3; Tables S4 and S5), we can also find there are large differences between SMAP data and in-situ SSM observations for a few sites, which are mainly from the regions where SMAP show potential errors discussed above, like the site COLDFOOT (SNOTEL network) where the surface temperature is low and the Maricao Forest (SCAN network) where the vegetation is dense. Since the MSE of gap-filled SMAP is close to (or even better than) the original SMAP data, the large validation errors of gap-filled SMAP for these sites are mainly due to the SMAP biases rather than the gap-filling process.

To analyze these uncertainties from SMAP, we mask the regions where SMAP data may have potential errors for the comparisons between models and observations (Figure S11). These regions are indicated as dense vegetation cover (vegetation water content >5 kg/m^2), frozen landscapes (surface temperature <0°C), and the presence of water bodies (water body fraction >5% coverage of a pixel), which is similar to a previous study (McColl et al., 2017). From our previous results, the differences of SSM_n between SMAP and CMIP5 models are larger in regions near the equator and higher latitudes if considering all of them as model biases (Figure 5). From Figure S11, we further find that these are also regions where SMAP data are likely less accurate, indicating that SMAP biases may also contribute to the inconsistency SSM_n difference from the latitudinal perspective. In addition, based on this SMAP masking, we further evaluate the correlations between the SSM_n multimodel differences without these regions and passing an 80% significance test with $\overline{Veg_n}$, $\overline{T_n}$, $\overline{Sand_n}$, and $\overline{Clay_n}$ (Figure 7; see Figure S12 as the same analysis but with differences passing a 100% significance test). We can see that, without the regions where the quality of SMAP data can not be guaranteed, the multimodel differences of SSM_n are still more correlated to climate conditions (i.e., vegetation water content and surface temperature) than soil texture (i.e., sand content and clay content), which is consistent with our previous results (Figure 6).

4. Conclusions

This study evaluates 17 land surface models from CMIP5 in simulating SSM variability based on SMAP SSM observations on global scales. We find that these models within CMIP5 generally underestimate SSM variability in higher frequency bands (weekly to seasonal) and overestimate SSM variability in the lower frequency band (seasonal to annual) compared to SMAP observations over the regions where SMAP are likely more accurate (such as less-vegetated and non-frozen areas). Besides, both the underestimation and overestimation concentrate in wetter regions with higher SSM content.

These multimodel differences are further found to be spatiotemporally different. From the temporal aspect, there is a higher variance on shorter time scales and a lower variance on longer time scales, suggesting an individual deficiency in representing short-term variability and a systematic deficiency of long-term variability in these models. Besides, this change can be clearly indicated by the seasonal time scale, indicating that the seasonal prediction is challenging for SSM simulation. From the spatial aspect, these multimodel differences have a more significant correlation with the mean vegetation water content and surface temperature than with soil texture on global scales, representing the climate condition is more important in evaluating SSM variability. For those differences that are more difficult to resolve, like SSM variability in the higher latitudes of the northern hemisphere

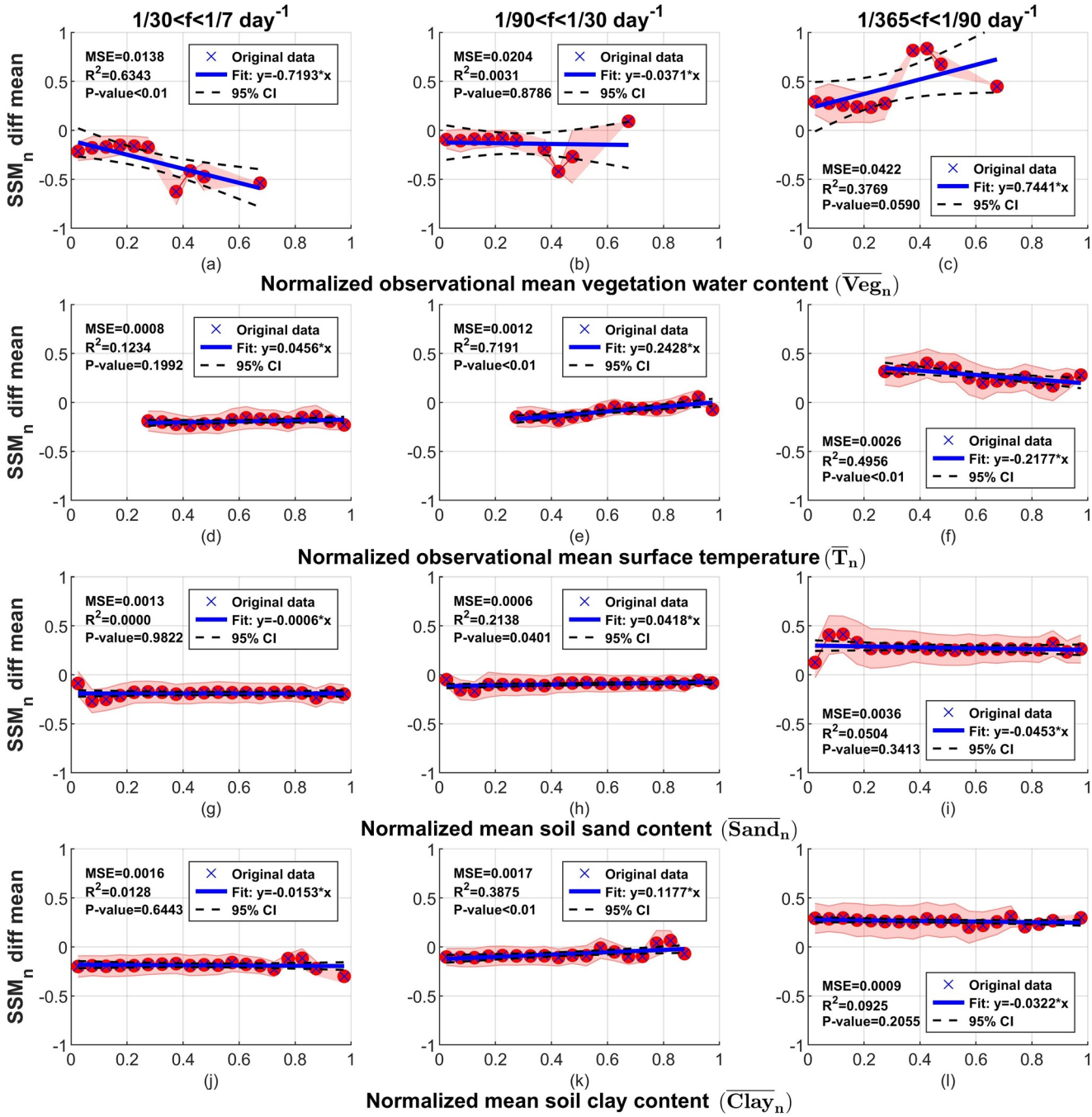

Figure 7. Same as Figure 6 except removing the regions within multimodel differences of SSM_n where SMAP data may have potential error sources. Differences in this figure are the values passing an 80% significance test. All values in the regions with $\overline{SSM}_n$ less than 0.1 are removed.

and in the regions with dense vegetation cover, apart from the need for more accurate satellite observations, the critical physical processes should not be simply parameterized in models but discover governing equations of the dynamical system, which could be achieved using physics-guided machine learning if data is abundant but the mechanisms remain elusive (Willard et al., 2020).

This study identifies systematic metrics of SSM that can be used to evaluate model improvements spatiotemporally based on remote sensing observations. It also highlights that the land surface models within CMIP5 should improve their capability to represent the temporal variability of soil moisture.

Data Availability Statement

The codes and data for analysis in this study are available at https://purr.purdue.edu/publications/3908/1.

Acknowledgments
The land surface models from CMIP5 were available online (https://esgf-node.llnl.gov/). SMAP data can be obtained on https://earthdata.nasa.gov/. ISMN data can be accessed on https://ismn.geo.tuwien.ac.at/en/. The long term global daily soil moisture dataset derived from AMSR-E and AMSR2 can be accessed on https://data.tpdc.ac.cn/en/data/c26201fc-526c-465d-bae7-5f02fa49d738/. The GSDE soil data were also available online (http://globalchange.bnu.edu.cn/research/soilw). Gentine acknowledges funding from NASA 80NSSC18K0998. Zhuang was funded by NASA through a subcontract from JPL #1609311.

References

Berg, A., & Sheffield, J. (2018). Soil moisture-evapotranspiration coupling in CMIP5 models: Relationship with simulated climate and projections. *Journal of Climate*, *31*(12), 4865–4878.

Bonan, G. B. (1996). *Land surface model (LSM version 1.0) for ecological, hydrological, and atmospheric studies: Technical description and users guide*. Technical note (No. PB-97-131494/XAB; NCAR/TN-417-STR). Climate and Global Dynamics Div. National Center for Atmospheric Research.

Botter, G., Peratoner, F., Porporato, A., Rodriguez-Iturbe, I., & Rinaldo, A. (2007). Signatures of large-scale soil moisture dynamics on streamflow statistics across US climate regimes. *Water Resources Research*, *43*(11).

Bourke, P. (1998). *Generating noise with different power spectra laws*.

Brodzik, M. J., Billingsley, B., Haran, T., Raup, B., & Savoie, M. H. (2012). EASE-Grid 2.0: Incremental but significant improvements for Earth-gridded data sets. *ISPRS International Journal of Geo-Information*, *1*(1), 32–45.

Burgin, M. S., Colliander, A., Njoku, E. G., Chan, S. K., Cabot, F., Kerr, Y. H., et al. (2017). A comparative study of the SMAP passive soil moisture product with existing satellite-based soil moisture products. *IEEE Transactions on Geoscience and Remote Sensing*, *55*(5), 2959–2971.

Chan, S. K., Bindlish, R., O'Neill, P., Jackson, T., Njoku, E., Dunbar, S., et al. (2018). Development and assessment of the SMAP enhanced passive soil moisture product. *Remote Sensing of Environment*, *204*, 931–941.

Chan, S. K., Bindlish, R., O'Neill, P. E., Njoku, E., Jackson, T., Colliander, A., et al. (2016). Assessment of the SMAP passive soil moisture product. *IEEE Transactions on Geoscience and Remote Sensing*, *54*(8), 4994–5007.

Chen, F., Crow, W. T., Bindlish, R., Colliander, A., Burgin, M. S., Asanuma, J., & Aida, K. (2018). Global-scale evaluation of SMAP, SMOS and ASCAT soil moisture products using triple collocation. *Remote Sensing of Environment*, *214*, 1–13.

Colliander, A., Jackson, T. J., Bindlish, R., Chan, S., Das, N., Kim, S. B., et al. (2017). Validation of SMAP surface soil moisture products with core validation sites. *Remote Sensing of Environment*, *191*, 215–231.

Colliander, A., Reichle, R., Crow, W., Cosh, M. H., Chen, F., Chan, S. K., et al. (2021). Validation of soil moisture data products from the NASA SMAP mission. *IEEE Journal of Selected Topics in Applied Earth Observations and Remote Sensing*.

Delworth, T. L., & Manabe, S. (1988). The influence of potential evaporation on the variabilities of simulated soil wetness and climate. *Journal of Climate*, *1*(5), 523–547.

Dirmeyer, P. A., Jin, Y., Singh, B., & Yan, X. (2013). Trends in land-atmosphere interactions from CMIP5 simulations. *Journal of Hydrometeorology*, *14*(3), 829–849.

Dorigo, W. A., Wagner, W., Hohensinn, R., Hahn, S., Paulik, C., Xaver, A., et al. (2011). The International Soil Moisture Network: A data hosting facility for global in situ soil moisture measurements. *Hydrology and Earth System Sciences*, *15*(5), 1675–1698.

Dorigo, W. A., Xaver, A., Vreugdenhil, M., Gruber, A., Hegyiova, A., Sanchis-Dufau, A. D., et al. (2013). Global automated quality control of in situ soil moisture data from the International Soil Moisture Network. *Vadose Zone Journal*, *12*(3).

Entekhabi, D., Njoku, E. G., O'Neill, P. E., Kellogg, K. H., Crow, W. T., Edelstein, W. N., et al. (2010). The soil moisture active passive (SMAP) mission. *Proceedings of the IEEE*, *98*(5), 704–716.

Entekhabi, D., Yueh, S., & De Lannoy, G. (2014). *SMAP handbook*.

Ghannam, K., Nakai, T., Paschalis, A., Oishi, C. A., Kotani, A., Igarashi, Y., et al. (2016). Persistence and memory timescales in root-zone soil moisture dynamics. *Water Resources Research*, *52*(2), 1427–1445.

Green, J. K., Seneviratne, S. I., Berg, A. M., Findell, K. L., Hagemann, S., Lawrence, D. M., & Gentine, P. (2019). Large influence of soil moisture on long-term terrestrial carbon uptake. *Nature*, *565*(7740), 476.

Guillod, B. P., Orlowsky, B., Miralles, D. G., Teuling, A. J., & Seneviratne, S. I. (2015). Reconciling spatial and temporal soil moisture effects on afternoon rainfall. *Nature Communications*, *6*, 6443.

Houska, T., Kraft, P., Chamorro-Chavez, A., & Breuer, L. (2015). SPOTting model parameters using a ready-made python package. *PLoS One*, *10*(12), e0145180.

Huang, Y., Gerber, S., Huang, T., & Lichstein, J. W. (2016). Evaluating the drought response of CMIP5 models using global gross primary productivity, leaf area, precipitation, and soil moisture data. *Global Biogeochemical Cycles*, *30*(12), 1827–1846.

Katul, G. G., Porporato, A., Daly, E., Oishi, A. C., Kim, H. S., Stoy, P. C., et al. (2007). On the spectrum of soil moisture from hourly to interannual scales. *Water Resources Research*, *43*(5).

Kennedy, D., Swenson, S., Oleson, K. W., Lawrence, D. M., Fisher, R., Lola da Costa, A. C., & Gentine, P. (2019). Implementing plant hydraulics in the community land model, version 5. *Journal of Advances in Modeling Earth Systems*, *11*(2), 485–513.

Kerr, Y. H., Waldteufel, P., Wigneron, J. P., Martinuzzi, J. A. M. J., Font, J., & Berger, M. (2001). Soil moisture retrieval from space: The soil moisture and Ocean Salinity (SMOS) mission. *IEEE Transactions on Geoscience and Remote Sensing*, *39*(8), 1729–1735.

Kim, H., Wigneron, J. P., Kumar, S., Dong, J., Wagner, W., Cosh, M. H., et al. (2020). Global scale error assessments of soil moisture estimates from microwave-based active and passive satellites and land surface models over forest and mixed irrigated/dryland agriculture regions. *Remote Sensing of Environment*, *251*, 112052.

Koster, R. D., Dirmeyer, P. A., Guo, Z., Bonan, G., Chan, E., Cox, P., et al. (2004). Regions of strong coupling between soil moisture and precipitation. *Science*, *305*(5687), 1138–1140.

Koster, R. D., Guo, Z., Yang, R., Dirmeyer, P. A., Mitchell, K., & Puma, M. J. (2009). On the nature of soil moisture in land surface models. *Journal of Climate*, *22*(16), 4322–4335.

Koster, R. D., & Suarez, M. J. (2001). Soil moisture memory in climate models. *Journal of Hydrometeorology*, *2*(6), 558–570.

Kumar, S. V., Dirmeyer, P. A., Peters-Lidard, C. D., Bindlish, R., & Bolten, J. (2018). Information theoretic evaluation of satellite soil moisture retrievals. *Remote Sensing of Environment*, *204*, 392–400.

Levine, P. A., Randerson, J. T., Swenson, S. C., & Lawrence, D. M. (2016). Evaluating the strength of the land-atmosphere moisture feedback in Earth system models using satellite observations. *Hydrology and Earth System Sciences*, *20*(12), 4837–4856.

McColl, K. A., He, Q., Lu, H., & Entekhabi, D. (2019). Short-term and long-term surface soil moisture memory time scales are spatially anticorrelated at global scales. *Journal of Hydrometeorology*, *20*(6), 1165–1182.

McColl, K. A., Wang, W., Peng, B., Akbar, R., Short Gianotti, D. J., Lu, H., et al. (2017). Global characterization of surface soil moisture drydowns. *Geophysical Research Letters*, *44*(8), 3682–3690.

Mudelsee, M. (2013). *Climate time series analysis*. Springer.
Nakai, T., Katul, G. G., Kotani, A., Igarashi, Y., Ohta, T., Suzuki, M., & Kumagai, T. O. (2014). Radiative and precipitation controls on root zone soil moisture spectra. *Geophysical Research Letters*, *41*(21), 7546–7554.
O'Neill, P., Bindlish, R., Chan, S., Njoku, E., & Jackson, T. (2018). *Algorithm Theoretical Basis Document. Level 2 & 3 soil moisture (passive) data products*.
O'Neill, P. E., Chan, S., Njoku, E. G., Jackson, T., Bindlish, R., & Chaubell, J. (2020). *SMAP L3 radiometer global daily 36 km EASE-grid soil moisture, Version 7*. NASA National Snow and Ice Data Center Distributed Active Archive Center. https://doi.org/10.5067/HH4SZ2PXSP6A
Ruane, A. C., & Roads, J. O. (2007). 6-Hour to 1-year variance of five global precipitation sets. *Earth Interactions*, *11*(11), 1–29.
Ruosteenoja, K., Markkanen, T., Venäläinen, A., Räisänen, P., & Peltola, H. (2018). Seasonal soil moisture and drought occurrence in Europe in CMIP5 projections for the 21st century. *Climate Dynamics*, *50*(3), 1177–1192.
Seneviratne, S. I., Corti, T., Davin, E. L., Hirschi, M., Jaeger, E. B., Lehner, I., et al. (2010). Investigating soil moisture-climate interactions in a changing climate: A review. *Earth-Science Reviews*, *99*(3–4), 125–161.
Seneviratne, S. I., & Koster, R. D. (2012). A revised framework for analyzing soil moisture memory in climate data: Derivation and interpretation. *Journal of Hydrometeorology*, *13*(1), 404–412.
Seneviratne, S. I., Koster, R. D., Guo, Z., Dirmeyer, P. A., Kowalczyk, E., Lawrence, D., et al. (2006). Soil moisture memory in AGCM simulations: Analysis of global land-atmosphere coupling experiment (GLACE) data. *Journal of Hydrometeorology*, *7*(5), 1090–1112.
Shangguan, W., Dai, Y., Duan, Q., Liu, B., & Yuan, H. (2014). A global soil data set for earth system modeling. *Journal of Advances in Modeling Earth Systems*, *6*(1), 249–263.
Taylor, K. E., Stouffer, R. J., & Meehl, G. A. (2012). An overview of CMIP5 and the experiment design. *Bulletin of the American Meteorological Society*, *93*(4), 485–498.
Thomson, R. E., & Emery, W. J. (2014). *Data analysis methods in physical oceanography*. Newnes.
Tuttle, S., & Salvucci, G. (2016). Empirical evidence of contrasting soil moisture-precipitation feedbacks across the United States. *Science*, *352*(6287), 825–828.
Ukkola, A. M., Pitman, A. J., De Kauwe, M. G., Abramowitz, G., Herger, N., Evans, J. P., & Decker, M. (2018). Evaluating CMIP5 model agreement for multiple drought metrics. *Journal of Hydrometeorology*, *19*(6), 969–988.
Wei, J., Dirmeyer, P. A., & Guo, Z. (2010). How much do different land models matter for climate simulation? Part II: A decomposed view of the land-atmosphere coupling strength. *Journal of Climate*, *23*(11), 3135–3145.
Weisstein, E. (2019). *"Parseval's theorem" from MathWorld—A Wolfram web resource*. Retrieved from http://mathworld.wolfram.com/ParsevalsTheorem.html
Willard, J., Jia, X., Xu, S., Steinbach, M., & Kumar, V. (2020). *Integrating physics-based modeling with machine learning: A survey*. arXiv preprint arXiv:2003.04919.
Williams, C. J. R., Allan, R. P., & Kniveton, D. R. (2012). Diagnosing atmosphere-land feedbacks in CMIP5 climate models. *Environmental Research Letters*, *7*(4), 044003.
Wrona, E., Rowlandson, T. L., Nambiar, M., Berg, A. A., Colliander, A., & Marsh, P. (2017). Validation of the Soil Moisture Active Passive (SMAP) satellite soil moisture retrieval in an Arctic tundra environment. *Geophysical Research Letters*, *44*(9), 4152–4158.
Xia, Y., Ek, M. B., Wu, Y., Ford, T., & Quiring, S. M. (2015). Comparison of NLDAS-2 simulated and NASMD observed daily soil moisture. Part I: Comparison and analysis. *Journal of Hydrometeorology*, *16*(5), 1962–1980.
Yao, P., & Lu, H. (2020). *A long term global daily soil moisture dataset derived from AMSR-E and AMSR2 (2002–2020)*. National Tibetan Plateau Data Center. CSTR: 18406.11.Soil.tpdc.270960. https://doi.org/10.11888/Soil.tpdc.270960
Yao, P., Lu, H., Shi, J., Zhao, T., Yang, K., Cosh, M. H., et al. (2021). A long term global daily soil moisture dataset derived from AMSR-E and AMSR2 (2002–2019). *Scientific Data*, *8*(1), 1–16.
Yao, P. P., Shi, J. C., Zhao, T. J., Lu, H., & Al-Yaari, A. (2017). Rebuilding long time series global soil moisture products using the neural network adopting the microwave vegetation index. *Remote Sensing*, *9*(1), 35.
Yuan, S., & Quiring, S. M. (2017). Evaluation of soil moisture in CMIP5 simulations over the contiguous United States using in situ and satellite observations. *Hydrology and Earth System Sciences*, *21*(4), 2203–2218.
Yuan, S., Quiring, S. M., & Leasor, Z. T. (2021). Historical changes in surface soil moisture over the contiguous United States: An assessment of CMIP6. *Geophysical Research Letters*, *48*(1), e2020GL089991.

References From the Supporting Information

Cochran, W. T., Cooley, J. W., Favin, D. L., Helms, H. D., Kaenel, R. A., Lang, W. W., et al. (1967). What is the fast Fourier transform? *Proceedings of the IEEE*, *55*(10), 1664–1674.
Cooley, J. W., & Tukey, J. W. (1965). An algorithm for the machine calculation of complex Fourier series. *Mathematics of Computation*, *19*(90), 297–301.
D'odorico, P., Laio, F., Porporato, A., & Rodriguez-Iturbe, I. (2003). Hydrologic controls on soil carbon and nitrogen cycles. II. A case study. *Advances in Water Resources*, *26*(1), 59–70.
Gentleman, W. M., & Sande, G. (1966). Fast Fourier transforms: For fun and profit. In *Proceedings of the November 7–10, 1966, fall joint computer conference* (pp. 563–578).
Gilman, D. L., Fuglister, F. J., & Mitchell, J. M., Jr. (1963). On the power spectrum of "red noise". *Journal of the Atmospheric Sciences*, *20*(2), 182–184.
Kay, S. M., & Marple, S. L. (1981). Spectrum analysis—A modern perspective. *Proceedings of the IEEE*, *69*(11), 1380–1419.
Mandelbrot, B. B. (1982). *The fractal geometry of nature* (Vol. 2). WH Freeman.
May, W., Meier, A., Rummukainen, M., Berg, A., Chéruy, F., & Hagemann, S. (2015). Contributions of soil moisture interactions to climate change in the tropics in the GLACE-CMIP5 experiment. *Climate Dynamics*, *45*(11), 3275–3297.
Melillo, J. M., McGuire, A. D., Kicklighter, D. W., Moore, B., Vorosmarty, C. J., & Schloss, A. L. (1993). Global climate change and terrestrial net primary production. *Nature*, *363*(6426), 234–240.
Steele, J. H. (1985). A comparison of terrestrial and marine ecological systems. *Nature*, *313*(6001), 355.
Vasseur, D. A., & Yodzis, P. (2004). The color of environmental noise. *Ecology*, *85*(4), 1146–1152.